

# Wireless Physical-Layer Identification: Modeling and Validation

Wenhao Wang, *Student Member, IEEE*, Zhi Sun, *Member, IEEE*,  
Kui Ren, *Fellow, IEEE*, Bocheng Zhu, and Sixu Piao

**Abstract**—The wireless physical-layer identification (WPLI) techniques utilize the unique features of the physical waveforms of wireless signals to identify and classify authorized devices. As the inherent physical layer features are difficult to forge, WPLI is deemed as a promising technique for wireless security solutions. However, as of today it still remains unclear whether existing WPLI techniques can be applied under real-world requirements and constraints. In this paper, through both theoretical modeling and experiment validation, the reliability and differentiability of WPLI techniques are rigorously evaluated, especially under the constraints of state-of-art wireless devices, real operation environments, as well as wireless protocols and regulations. Specifically, a theoretical model is first established to systematically describe the complete procedure of WPLI. More importantly, the proposed model is then implemented to thoroughly characterize various WPLI techniques that utilize the spectrum features coming from the non-linear RF-front-end, under the influences from different transmitters, receivers, and wireless channels. Subsequently, the limitations of existing WPLI techniques are revealed and evaluated in details using both the developed theoretical model and in-lab experiments. The real-world requirements and constraints are characterized along each step in WPLI, including i) the signal processing at the transmitter (device to be identified), ii) the various physical layer features that originate from circuits, antenna, and environments, iii) the signal propagation in various wireless channels, iv) the signal reception and processing at the receiver (the identifier), and v) the fingerprint extraction and classification at the receiver.

## I. INTRODUCTION

In wireless communications, physical waveforms transmitted by any wireless device are inherently stamped with unique features in the physical layer of the communication, which can be utilized to identify impostors and classify authorized users. Such device identification solutions are defined as Wireless Physical-Layer Identification (WPLI) techniques [1], which are meanwhile utilized in the area of Physical-layer Security [2], [3], [4]. While the conventional software-level device identifications (e.g., IP or MAC address) can be easily changed by malwares, the physical layer feature cannot be modified without significant effort. Therefore, the WPLI technique is deemed as a promising wireless security solution, if the physical layer features, or the so called "radio frequency fingerprints

Wenhao Wang and Zhi Sun are with the Department of Electrical Engineering, Kui Ren and Sixu Piao are with Department of Computer Science and Engineering, University at Buffalo, the State University of New York, Buffalo, NY 14260, United States. E-mail: {wenhaowa, zhisun, kuiren, sixupiao}@buffalo.edu. Wenhao Wang and Bocheng Zhu are with School of Electronics Engineering and Computer Science, Peking University, Beijing 100871, China, Email: {wenhaowang, zhucb}@pku.edu.cn.

Zhi Sun's research is supported in part by the US NSF under Grant CNS-1547908. Kui Ren's research is supported in part by the US NSF under grant CNS-1318948. Wenhao Wang's jointly training PhD program is supported by China Scholarship Council.

(RFFs)", are sufficiently reliable and distinguishable. The question is: are RFFs reliable and distinguishable in real and practical applications? Or more specifically, given state-of-art wireless devices and in real operation environments, can WPLI techniques reliably and uniquely identify/classify the authorized users and impostors? The objective of this paper is to answer the question.

To analyze the reliability and differentiability of RFFs, the origins of various RFFs need to be point out first. Fig. 1 illustrate the logic procedure of WPLI during the wireless communication between a transmitter (the device to be identified) and a receiver (the identifier). The RFFs can come from many points along that procedure. At the transmitter side, the RFFs are rooted in the hardware imperfections of the transmitter device [1], which include clock jitter [5], [6], the DAC sampling error [7], the mixer or local frequency synthesizer [8], [9], the power amplifier non-linearity [7], [10], [11], device antenna [12], modulator sub-circuit (if the analog modulation is used) [13], among others. The RFF-stamped signals are then radiated by the transmitter antenna to the wireless channel, where another type of RFFs are added to the physical waveform, i.e., the unique multipath wireless link characteristics [2], [14]. At the receiver (i.e., the identifier), the signals are received by the receiver antenna and processed through the analog circuits and digital processing units. Depends on their properties, different RFFs are extracted at (i) different parts of the signals, such as turn-on/off transient [9], [15], [16], [17]; data [5], [12], [18], [19], [20], and clock [5], [6], and (ii) different domains, such as time [13], frequency [12], [15], and wavelet domains [21]. Some works extract multiple features from different parts of signal to form a combined RFF. For instance, In [22], carrier frequency difference, phase shift difference and second-order cyclostationary feature, amplitude of OFDM signal are exploited integratedly. Finally the extracted RFF is matched with the fingerprint database, which complete the physical-layer identification process.

According to the procedure of WPLI, the factors that can influence the reliability and differentiability of RFFs include: (i) the signal preparing procedure (e.g., modulation and shaping filter) at the transmitter before the RFF is added; (ii) the characteristics of the various hardware imperfections at the transmitter; (iii) the characteristics of the multipath wireless channel and the influence of the operation environments; (iv) the signal reception and processing procedure at the receiver; and (v) the fingerprint extraction and matching strategy at the receiver. Although the reported error rate of many existing WPLI solutions are impressive (single-digit % error rate), most existing works use oscilloscopes or spectrum analyzers as the

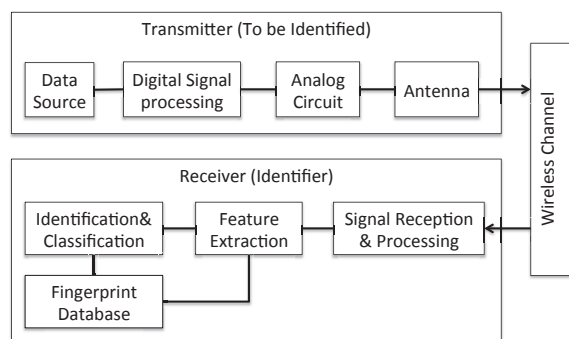


Fig. 1. The logic procedure in wireless physical-layer identification.

identifier [5], [12], [15], which has orders of magnitude higher sampling rate than real wireless receivers (e.g., smart phones or wireless sensors). In addition, most reported WPLI results are derived in open space with an ideal and fixed wireless channel [5], [15]. Some works even just place the receiver right beside the transmitter [12]. In fact, practical wireless channel (especially the multipath channel, which is dominant in indoor and metropolitan environments) are highly dynamic and can dramatically distort the transmitted signals as well as the RFF. Moreover, most existing WPLI solutions require updating RFF database each time when the wireless users or obstructions move or the WPLI system is placed in a new environment. However, mobility is the fundamental requirement of most current wireless applications. It is highly impractical if the identifier has to rebuild the RFF database whenever the users move.

To address the concern on the reliability and differentiability of RFFs, the modeling and evaluation of the existing WPLI solutions under the influence of the above real-world limitations is of great importance. However, the research in this field is still very limited. There is still no clear answer on whether existing WPLI techniques can fulfill the above five criteria. In [7] and [10], the RF-front-end-based RFF is modeled as nonlinear distortions at the transmitter. Then a hypothesis test-based theoretical model is provided to evaluate the identification accuracy. However, the impacts of receiver device and the wireless channel are not considered. Moreover, while the model provides simple and neat theoretical prediction, it cannot capture the effects of the complex procedures in signal processing procedure of the wireless communication and the fingerprint extraction/match. In [20], the influence of the low-end wireless receiver is evaluated through experiments. However, this experiment-based work is limited to one type of devices in one channel, which lacks the universal insights. Similarly, in [15], the stability of the identification accuracy is investigated by experiments in the wireless channel with varied distances and antenna polarizations. The specific-channel experiments also lack the applicability to other wireless environments.

Currently, to our best knowledge, there is no work that provides a systematic understanding and quantitatively evaluation of the whole WPLI procedure under the aforementioned real-world limitations. In this paper, through a comprehensive theoretical model and a series of experiments, we rigorously evaluate the reliability and differentiability of WPLI tech-

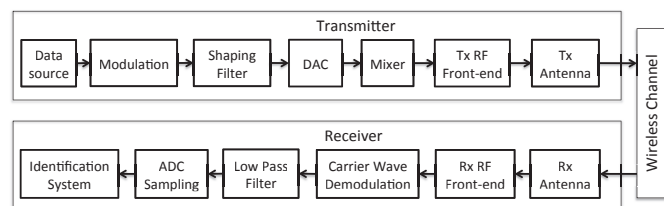


Fig. 2. WPLI procedure along wireless communication flow block diagram.

niques according to the aforementioned five criteria. First, we develop a WPLI model that provides a systematic and mathematic description of the whole WPLI procedure. More importantly, we then implement the developed model in various WPLI systems that use the spectrum domain RFF due to the non-linear RF front-end. The performance and limitations of that WPLI system is quantitatively evaluated according to our five criteria in different settings of receiver device, wireless channel, and communication protocol. We select the spectrum domain RFF from non-linear RF front-end as the study case because it has relatively low requirement of the receiver hardware while gives very good reported performance. The influence of real-world requirements and constraints are analyzed along each step in the inter-coupled WPLI and wireless communications. We conduct in-lab experiments to validate the developed model and our findings using the off-the-shelf wireless devices. We use the MicaZ sensors as the transmitter (device to be identified) and USRP as the receiver (identifier), which are deployed in several specially designed indoor multipath fading channels. The influence of multiple factors on WPLI also are tested.

The reminder of this paper is organized as follows. The theoretical model is developed to characterize the complete WPLI procedure in Section II. This section provides general but rigorous theoretical modeling of the whole WPLI procedure, including four major segments: the signal processing and RFF stamping at the transmitter, the signal propagation along wireless channels, the signal reception and feature extraction at the receiver, and the final identification and classification. Then, in Section III, the limitations of WPLI are analyzed in details by implementing the theoretical model in various WPLI systems where the RFFs come from the RF-front-end non-linearity. The real-world requirements and constraints of the major segments modeled in previous section, are analyzed with specific application cases. Next, we further validate and discuss our findings by experiments in Section IV. The the influence of major factors emphasized in previous sections, are analyzed through a series of experiments. Finally, the paper is concluded in Section V.

## II. THEORETICAL MODEL OF WPLI

As the WPLI is closely coupled with wireless communications, the theoretical model of WPLI is also based on the wireless communication procedure, as shown in Fig. 2. This section provide general but rigorous mathematical descriptions of the whole WPLI procedure.

### A. Signal Processing and RFF Stamping at Transmitter

At beginning of the signal processing at the transmitter, the data source send binary bits sequence to the digital modulation

block, where the sequential binary bits are first mapped to higher order and complex transmit symbols. We use  $m$  to index the sequence of the transmitted symbols so that each symbol is denoted as  $x_m = x_m^I + jx_m^Q$ , where  $x_m^I$  and  $x_m^Q$  are the in-phase and quadrature components, respectively. The duration of each symbol is determined by the expected data rate and the order of modulation scheme, which is denoted as  $T_{symbol}$ . Ideally,  $T_{symbol}$  should be a constant in one packet transmission. However, due to the clock-related hardware imperfection, the period/duration of each symbol can vary. As a result, the first possible RFF due to the hardware imperfection appears, which is regarded as a unique time domain feature and is defined as time interval error (TIE) [5]. We denote this feature as  $\sigma_{TIE}^m$  at the  $m^{th}$  symbol. Hence, the real symbol duration of the  $m^{th}$  symbol becomes  $T_m = T + \sigma_{TIE}^m$ .

After that the complex symbols  $x_m$  is processed by the shaping filter  $h_s(t, T_m)$ , which gives the output  $b_{mod}(x_m, h_s(t, T_m))$ , where the formulation of the function  $b_{mod}(\cdot)$  is determined by the specific modulation scheme (we will discuss several examples in Section III). Then the digital signal moves to the digital-to-analog converter (DAC). It should be noted that  $b_{mod}(x_m, h_s(t, T_m))$  is in fact a discrete function as the digital shaping filter  $h_s(t)$  only change value when the DAC generate new output. We consider that the DAC has a generation period  $T_g$ , i.e., the DAC converts the value of  $b_{mod}(x_m, h_s(t, T_m))$  to analog current every  $T_g$  second. Then the input digital signal  $u[n]$  (indexed by  $n$ ) at the DAC can be expressed as

$$u[n] = A \sum_m b_{mod}(x_m, h_s(nT_g - mT_m, T_m)), \quad (1)$$

where  $A$  is the amplitude coefficient. It should be noted that the clock-related hardware imperfection could also influence the DAC generation period  $T_g$ . However, since  $T_g$  is much smaller than  $T_m$  (due to the high DAC sampling rate), the TIE in  $T_g$  is much less significant and can be neglected. It is also worth mentioning that any specific wireless protocol (e.g., 802.11, 802.15, GSM/GPRS, etc.) defines particular modulation schemes and shaping filter, which prepare the transmitted signal with different bandwidth and power spectrum density (PSD). Those parameters can dramatically influence the significance of RFF and eventually affect the performance of WPLI. Detailed examples are discussed in Section III and IV.

Ideally the DAC converts the baseband signal sequence  $u[n]$  to a time-continuous analog signal  $u(t)$ . However, the real output signal  $y_u(t)$  from practical DAC is combed with quantization error and integral nonlinearity (INL) [23], which can be expressed as

$$y_u(t) = \sum_{n=-\infty}^{\infty} (u(n) + \Delta_n) g\left(\frac{t-nT_g}{T_g}\right) + \Delta_{INL},$$

$$g(\theta) = \begin{cases} 1, & 0 \leq \theta < 1 \\ 0, & \text{elsewhere} \end{cases} \quad (2)$$

where  $\Delta_n$  is quantization noise, for  $M$ -bit DAC quantization with input signal dynamic range  $[-U, U]$ , the maximum quantization error  $\delta_\Delta = 2^{-M}U$ ,  $\Delta_{INL}$  is the integral nonlinearity that is also regarded as a unique feature rooted in hardware imperfection in [7].

After the DAC, the analog baseband signal is moved to passband by the mixer. Ideally the complex passband signal

$z(t)$  consists the in-phase component  $i(t) \cdot \cos(\omega_c t)$  and the quadrature component  $jq(t) \cdot \sin(\omega_c t)$ , where  $\omega_c$  is the carrier angle frequency and  $i(t) = \text{Re}\{y_u(t)\}$ ,  $q(t) = \text{Im}\{y_u(t)\}$ . However, in practical, the phase offset quadrature error occurs in this procedure due to the imperfection of transmitter's frequency synthesizers (local oscillators), which modifies  $z(t)$  to

$$z(t) = \frac{1}{2}(\text{Re}\{y_u(t)\} \cdot e^{j\zeta/2} + \text{Im}\{y_u(t)\} \cdot e^{-j\zeta/2}) \cdot e^{j\omega_c t} \\ + \frac{1}{2}(\text{Re}\{y_u(t)\} \cdot e^{j\zeta/2} - \text{Im}\{y_u(t)\} \cdot e^{-j\zeta/2}) \cdot e^{-j\omega_c t} \quad (3)$$

where  $\zeta$  is the quadrature error. In [9] and [8], the uniqueness of the mixer quadrature error is utilized as RFFs.

Finally, the passband signals go through the TX front-end amplifier and filter to gain enough power for radiation. In this procedure, another important RFF is stamped, i.e., the non-linearity of the front-end amplifier [24], which is widely used in many recent WPLI techniques [24], [7], [10], [11]. The output signal can be formulated as

$$w(t) = h_{PA}(z(t), \tilde{\mathbf{a}}_{tx}) \otimes h_{BP}(t)$$

$$H_{BP}(f) = \begin{cases} 1, & |f| < W_c \\ 0, & |f| > W_c \end{cases} \quad (4)$$

where  $h_{PA}(\cdot, \tilde{\mathbf{a}}_{tx})$  is nonlinear function of power amplifier at the transmitter (detailed examples are given in Section III);  $\tilde{\mathbf{a}}_{tx}$  is complex complex power-series,  $\otimes$  stands for convolution computing; and  $h_{BP}(t)$  is the bandpass filter function that is nearly ideal within the carrier bandwidth  $W_c$ .

## B. Signal Propagation between TX and RX Antennas along Wireless Channel

We consider the antennas as part of the wireless channel since both the antenna polarization and the multipath channel can be used as RFFs in WPLI. With the input signal  $w(t)$  given in (II-A), the intensity of the radiated EM waves by a polarized antenna is given by

$$\vec{A}_{tx}(t) = F_{tx}^h[w(t)] \cdot e^{-j\phi_{tx}^h} \cdot \vec{\rho}_h + F_{tx}^v[w(t)] \cdot e^{-j\phi_{tx}^v} \cdot \vec{\rho}_v \quad (5)$$

where  $\vec{\rho}_h$  and  $\vec{\rho}_v$  are the direction unit vectors in the horizontal and vertical directions, respectively;  $F_{tx}^h(\cdot)$  and  $F_{tx}^v(\cdot)$  are the TX antenna projection functions that project the input signal  $w(t)$  to the horizontal and vertical polarization, respectively;  $\phi_{tx}^h$  and  $\phi_{tx}^v$  are the polarization phases at both directions. In some specific wireless system, such as RFID using the spiral coil antenna, the imperfection of antenna hardware can also contribute to the RFF in WPLI [12]. Moreover, even for the simpler antennas that are widely used in contemporary wireless devices (e.g., dipole antennas and patch antennas), although the RFF does not come from antenna imperfection, the random direction of antenna can generate random polarization. Then the antenna polarization can either influence the RFFs due to other hardwares [15] or act as a new RFF (coupled with the multipath effect) [2], [14].

The radiated EM waves then propagate through the multipath wireless channel and finally reach the RX antenna at the receiver. As the RX antenna can be also polarized, the

intensity of the EM waves at the RX antenna is also presented in both horizontal and vertical direction:

$$\vec{A}_{rx}(t) = \sum_{i=1}^{N_p} \vec{A}_{tx}(t) \cdot (h_i^h \cdot \vec{\rho}_h + h_i^v \cdot \vec{\rho}_v) \otimes \delta(t - \tau_i) \quad (6)$$

where we consider there are  $N_p$  paths (including line-of-sight, reflected, diffracted, and refracted paths) connecting the transmitter and receiver;  $h_i^h$  and  $h_i^v$  are the path loss of the  $i^{th}$  path with horizontal polarized waves and vertical polarized waves, respectively;  $\tau_i$  is the propagation delay of the  $i^{th}$  path. It is obvious that the complex multipath wireless channel can arbitrarily change the amplitude, the delay, the phase of the EM waves at each single path. Consequently, the wireless channel can literally mask most, if not all, RFFs stamped at the transmitter. Hence, the channel effects on WPLI need special attention in the performance evaluation. In [1], [15], it has been proved that the WPLI accuracy decreases as the distance between the transmitter and receiver increases. It should be noted that the channels considered in [1], [15] are still friendly, which is open space without significant multipath and obstructions. The practical wireless channel, especially in real indoor or metropolitan environments, could be much more hostile in keeping the RFFs from the transmitter. We will do case studies in various multipath channels in the following sections.

### C. Signal Reception and Processing at Receiver

At the receiver, the RX antenna captures the EM waves (given in (6)) and convert both the horizontal and vertical polarized components to the received signal:

$$r(t) = F_{rx}^h \cdot \vec{A}_{rx}(t) \cdot \vec{\rho}_h \cdot e^{j\phi_{rx}^h} + F_{rx}^v \cdot \vec{A}_{rx}(t) \cdot \vec{\rho}_v \cdot e^{j\phi_{rx}^v}; \quad (7)$$

where  $F_{rx}^h(\cdot)^{-1}$  and  $F_{rx}^v(\cdot)^{-1}$  are the RX antenna functions that capture the horizontal and vertical EM wave components, respectively;  $\phi_{rx}^h$  and  $\phi_{rx}^v$  are the polarization phases of the RX antenna.

Similar as the transmitter, the received signal also need to pass through the RF front-end at the receiver:

$$f(t) = h_{PA}(\cdot, \vec{\mathbf{a}}_{rx}) \otimes h_{BP}(t), \vec{\mathbf{a}}_{rx} \quad (8)$$

where  $h_{PA}(\cdot, \vec{\mathbf{a}}_{rx})$  is nonlinear function of power amplifier at the receiver; and  $h_{BP}(t)$  is the bandpass filter at the receiver, all similar to the case at the transmitter.

Then the output signal from the RX front-end is convert to baseband by the receiver mixer with quadrature errors (i.e., carrier demodulation). The demodulation signal then goes through the low pass filter  $h_{LP}(t)$  to eliminate the higher frequency components, which gives the results of

$$x(t) = \frac{1}{2}(\text{Re}\{f(t)\} \cdot e^{j\zeta/2} + \text{Im}\{f(t)\} \cdot e^{-j\zeta/2}) \cdot e^{j\omega_c t} \otimes h_{LP}(t) \quad (9)$$

$$+ \frac{1}{2}(\text{Re}\{f(t)\} \cdot e^{j\zeta/2} - \text{Im}\{f(t)\} \cdot e^{-j\zeta/2}) \cdot e^{-j\omega_c t} \otimes h_{LP}(t)$$

Note that the low pass filter at the receiver always have a strict cutoff to control the noise level. The gains of the pass-band and stop-band can significantly affect the extracted RFFs, especially the spectrum-domain RFFs. The low pass filter function  $h_{LP}(t)$  can be modeled as

$$H_{LP}(f) = \begin{cases} A_p, & |f| < W \\ A_s, & |f| > W \end{cases} \quad (10)$$

where  $A_p$  and  $A_s$  are the gains in the pass-band and stop-band, respectively.

Finally, the received baseband signals  $x(t)$  are sampled by analog-to-digital converter (ADC) to obtain the digital signal sequences which are sent to the identification units to extract the fingerprints. The ADC output is expressed as

$$x[n] = x(nT_s) + \Delta_n \quad (11)$$

where  $\Delta_n$  is random quantization noise, for M-bit ADC quantization and input dynamic range  $[-V, V]$ , the maximum quantization error is  $\delta_\Delta = 2^{-M}V$ . As discussed in Section I, most existing WPLI solutions utilize the high-end measurement equipment (e.g., oscilloscope and spectrum analyzer) as the receiver. The key difference between the real wireless receivers lies in the sampling rate. While the oscilloscope and spectrum analyzer can directly sample the passband (or the baseband) signal at sampling rate in the order of GHz, most practical wireless device can only sample the baseband signal at the MHz rate. Hence, in the following sections, we will quantitatively analyze the important influence of the receiver's sampling rate.

It should be noted that the above signal reception and processing procedures are also subject to the influence of the hardware imperfections at the receiver's antenna, front end, mixer, and ADC. However, those hardware imperfections are known to the receiver (or the identifier). Hence, the deviation or errors introduced by those hardware imperfections at the receiver can be adjusted and corrected when RFF is extracted.

### D. RFF Extraction, Identification, and Classification

At the identification unit of the receiver, the RFFs are extracted from the sampled digital signals( $x[n]$  in (11)). The extracted feature can be expressed as

$$\mathbf{S} = \text{Feature}(\{x[n], n \in \mathbf{N}\}) \quad (12)$$

where  $\mathbf{N}$  is the set of all sampled digital signals in this round of identification;  $\text{Feature}(\cdot)$  is the feature extraction function. Depending on the properties of the RFF and the selected extraction strategy, the feature extraction function  $\text{Feature}(\cdot)$  usually consists of domain change (e.g., Fourier transform, Wavelet transform, Hilbert transform, among others) and dimensionality reduction (e.g., linear discriminant analysis (LDA), principal component analysis (PCA), or simply picking us a certain parameter such as modulation errors and phase errors).

By now, the RFF  $\mathbf{S}$  is obtained. The next step is to match the RFF with the reference fingerprint,  $\mathbf{S}_R$  to calculate the distance matching scores and make the classification or identification decisions. The performance of the classification/identification can be evaluated by the error probabilities, which can be theoretically calculated through hypothesis testing models.

1) *Classification*: For  $N$ -users classification scenario, we adopt  $N$ -hypothesis testing techniques to apply to  $N$  genuine users with  $M_N$  reference fingerprints in the database for each user [25]. The hypothesis  $\mathcal{H}_N$  is that the obtained signal is from the genuine user  $\#N$ . Then the classification probability can be expressed by  $P(\mathcal{H}_i|\mathcal{H}_j)$ ,  $i, j = 1, \dots, N, i \neq j$ , which is the probability that the RFF from genuine user  $\#j$  is classified

as the genuine user  $\#i$ . Such probability can be derived based on the feature distance between the extracted testing feature vector  $\mathbf{S}$  with the reference feature vector  $\mathbf{S}_R$ :

$$D_i(\mathbf{S}) = \text{Distance}(\mathbf{S}, \mathbf{S}_R) \quad (13)$$

The testing feature vector  $\mathbf{S}$  is matched with all the reference fingerprints and assigned to the identity with the smallest distance score. Then the classification error probability can be expressed as

$$P(\mathcal{H}_i|\mathcal{H}_j) = P(D_i = \min(\{D\})|\mathcal{H}_j); \quad (14)$$

where the formulation of the probability  $P(D_i = \min(\{D\})|\mathcal{H}_j)$  depends on the distribution of  $D_i(\mathbf{S})$ , which is discussed in detail in Section III. Then the average classification error rate can be derived:

$$P_e = \sum_{i=1}^N \sum_{j=1, j \neq i}^N P(\mathcal{H}_j|\mathcal{H}_i)P(\mathcal{H}_i) \quad (15)$$

2) *Identification*: Unlike the  $N$ -users classification, in the identification procedure, the distance scores between each authorized class is not the key metric. The whole network can be considered as a two-user hypothesis model [15], [7], [10].  $\mathcal{H}_1$  is the hypothesis that the incoming testing fingerprint is from the genuine users while  $\mathcal{H}_0$  indicates that the testing fingerprint is from an unknown imposter. In another word, all the  $N$  genuine users that have reference fingerprints stored in database can be treated as a whole class. A decision threshold  $\lambda$  is set up based on the calculated feature distance in (29). If the minimal distance score is larger than the threshold, the testing feature is identified as an imposter's fingerprint, i.e.,  $\mathcal{H}_0$ , otherwise it is judged as from a genuine user  $\mathcal{H}_1$ , i.e.,

$$\min(\{D\}) \underset{\mathcal{H}_1}{\overset{\mathcal{H}_0}{\geq}} \lambda. \quad (16)$$

To evaluate the accuracy of identification performance, several probability metrics can be applied [12], [15], including false accept rate (FAR)  $P(\mathcal{H}_1|\mathcal{H}_0)$ , false reject rate (FRR)  $P(\mathcal{H}_0|\mathcal{H}_1)$ , genuine accept rate (GAR)  $P(\mathcal{H}_1|\mathcal{H}_1)$ , and genuine reject rate (GRR)  $P(\mathcal{H}_0|\mathcal{H}_0)$ . Based on the decision rule given in (16), the above probabilities can be calculated in the same way as the classification case according to (13) and (14). We don't further elaborate the similar formulas here. To generate a single probability metric in identification system, many work put the above error rates together in the Receiver Operating Characteristic (ROC) chart where the FRRs (or GARs) are plotted as a function of different FAR levels. The operating point in ROC, where FAR and FRR are equal, is referred to as the equal error rate (EER).

### III. REAL-WORLD CONSTRAINS AND REQUIREMENTS: ANALYSIS BY IMPLEMENTING THE WPLI MODEL

In this section, we implement the developed WPLI model in a promising and widely adopted WPLI technique [18], [15], [12], [5], i.e., the WPLI using frequency domain RFF that originates from the non-linearity of the TX front-end amplifier. We select the frequency domain RFF as the case to study after the general modeling, due to two reasons: (i) it's widely used by the state-of-the-art WPLI solutions; and (ii) it contains

more information in various ways, which integrates amplitude, frequency, and phase all in a high dimensionality. In [5], the classification results also proves it shows the best performance. We choose the nonlinearity due to RF front-end, because it's the most significant and dominant transmitter genuine effects, which can directly result in the spectral regrowth of transmitted signal, as the discussion in [10], [11], [26]. The real-world requirements and constraints of the key procedures in WPLI are analyzed according to this application case.

#### A. Modulation and Shaping Filter: Constraints of Communication Protocols and Regulation

Preparing the transmitted signal through modulation and shaping filter are the first steps in the WPLI procedure in Fig. 2. In fact, the modulation and shaping filter are determined by the specific communication protocol to achieve the expected data rate and to keep the signal power staying within the assigned spectrum band (not interfere other wireless services). The RFF has to be stamped on the resulted signal. Hence, the regulated modulation and shaping filter become the first constraints on WPLI. As mentioned in (1), the function  $b_{mod}(\cdot)$  is determined by the specific modulation scheme and shaping filter. Here we implement two widely used modulation schemes: M-PSK and M-QAM. The modulation functions  $b_{mod}(\cdot)$  in (1) for M-PSK can be further expressed as

$$b_{PSK}(x_m, h_s(t)) = \exp\{j\frac{\pi}{M}x_m\}h_s(t), \quad (17)$$

$$x_m \in \{\pm 1, \pm 3, \dots, \pm(M-1)\};$$

where  $M$  is the modulation order. For M-QAM,

$$b_{QAM}(x_m, h_s(t)) = x_m h_s(t), \quad (18)$$

$$x_m \in \{\pm 1, \pm 3, \dots, \pm(N-1)\}, N = \sqrt{M}$$

Similarly, we implement two widely used shaping filters, including the half-sine (HS) and root-raised-cosine (RRC) filters. The HS shaping is utilized in IEEE 802.15.4 protocols and the RRC is used in GSM cellular systems. The shaping filter function  $h_s(t, T_m)$  in (1) can be further expressed as

$$h_{s,HS}(t, T_m) = \sin(\pi\frac{t}{2T_m}) \quad (19)$$

$$h_{s,RRC}(t, T_m) = 4\beta \frac{\cos((1+\beta)\pi t/T_m) + \sin((1-\beta)\pi t/T_m)/(4\beta t/T_m)}{\pi\sqrt{T_m}(1-(4\beta t/T_m)^2)} \quad (20)$$

$$0 < t < 2T_m,$$

where  $T_m$  is the duration of the  $m^{\text{th}}$  symbol and  $\beta$  is the rolloff factor of RRC shaping filter. After the implementing the specific modulation scheme and shaping filter, the output passband signal  $z(t)$  after the processing of the DAC and mixer along WPLI procedure in Fig. 2 can be analytically characterized. The power spectrum density (PSD) of  $z(t)$  using different modulation schemes and shaping filters can be numerically derived. We leave the conclusion of the influence of modulation scheme and shaping filter on RFFs to the next subsection where the RFF (i.e., the front-end non-linearity in this WPLI system) is added to the passband signal.

#### B. RF Front-end Non-linearity: Significance of Selected RFF

According to Fig. 2, the passband signal  $z(t)$  is amplified to gain enough radiation power at the RF front-end, where

the RFF considered in this section is added to the signal. The RFF is due to the nonlinear distortion and regrowth of the spectrum at the transmitter RF front-end amplifier, which can be characterized by a complex power-series behavioral model [27]. The spectrum of output signal of the RF front-end can be modeled as

$$S_{FE}(f) = \mathbf{H}(\mathbf{z}, \tilde{\mathbf{a}}_{\text{tx}}) = \sum_{n=0}^{\frac{(N-1)}{2}} \sum_{m=0}^{\frac{(N-1)}{2}} \frac{\tilde{a}_{2n+1} \tilde{a}_{2m+1}^*}{2^{2(n+m)}} \times \binom{2n+1}{n+1} \binom{2m+1}{m+1} \tilde{S}_{(2n+1)(2m+1)}(f); \quad (21)$$

where  $S_{FE}(f)$  is the output signal spectrum after the front-end;  $\tilde{\mathbf{a}}_{\text{tx}} = \{\tilde{a}_n\}$  is the set of the unique coefficients of the non-linear system;  $\tilde{S}_{(2n+1)(2m+1)}(f)$  is the  $N^{\text{th}}$  odd order autocorrelation spectrum of  $z(t)$ ;  $z(t)$  is the input passband signal; and  $*$  denotes the conjugate signal. The function  $\tilde{S}_{(2n+1)(2m+1)}(f)$  is given by

$$\tilde{S}_{(2n+1)(2m+1)}(f) = \int_{-\infty}^{\infty} \mathfrak{K}_{\tilde{z}_{2n+1} \tilde{z}_{2m+1}}(\tau) e^{-j\omega\tau} d\tau,$$

where

$$\mathfrak{K}_{\tilde{z}_{2n+1} \tilde{z}_{2m+1}}(\tau) = \lim_{T \rightarrow \infty} \int_{-T}^T \tilde{z}_1^{n+1}(\tilde{z}_1^*)^n \tilde{z}_1^m (\tilde{z}_2^*)^{m+1} dt, \\ \tilde{z}_1 = z(t), \quad \tilde{z}_2 = z(t + \tau),$$

Each non-linear RF front-end has a unique set  $\tilde{\mathbf{a}}_{\text{tx}}$  that constitutes the foundation of the RFF. In the theoretical modeling in this paper, we derive the coefficient set  $\tilde{\mathbf{a}}_{\text{tx}}$  by fitting the measured spectrum of the output signal of real wireless devices (MicaZ sensor nodes [28] and USRP software defined radio platform [29]). Note that the antennas in MicaZ sensors and USRPs are simple vertical polarized antennas. Hence, they can be considered as ideal single polarized antennas without obvious imperfection.

Now we can numerically check the significance of the selected RFF as well as the influence of modulation scheme and shaping filter. Fig. 3(a) - Fig. 3(d) show the PSDs of the transmitted wireless signal at the TX side with and without the RFF (front-end non-linearity), using different modulation schemes and shaping filters. The PSD without RFF is derived by our model with the ideal RF front-end. To derive the PSD with RFF, two non-linear system coefficient sets ( $\tilde{\mathbf{a}}_{\text{tx}}$ ) are derived based on the measurements from two USRP transmitters, which have the carrier frequency  $f_c = 2.48\text{GHz}$  (IEEE 802.15.4) and the fixed baseband data chip rate  $R_b = 2\text{Mbps}$ .

Fig. 3(a) shows the PSDs using OQPSK modulation and half-sine shaping filter. The PSDs with RFF are significantly different from the PSD without RFF. Moreover, the RFF-stamped PSDs of different devices also show obvious uniqueness, which confirms the effectiveness of the selected RFF (at least at the TX side before wireless channel). More importantly, we observe that RFF become more significant as the signal spectrum moves away from the carrier frequency. In another word, RFF is mainly added to the higher frequency segment of the baseband signal.

In Fig. 3(b), the shaping filter is changed from half-sine to RRC. We can see that the half-sine shaping filter can result in a spectrum with more side lobes and larger bandwidth, while the RRC shaping filter strictly restrains the bandwidth and

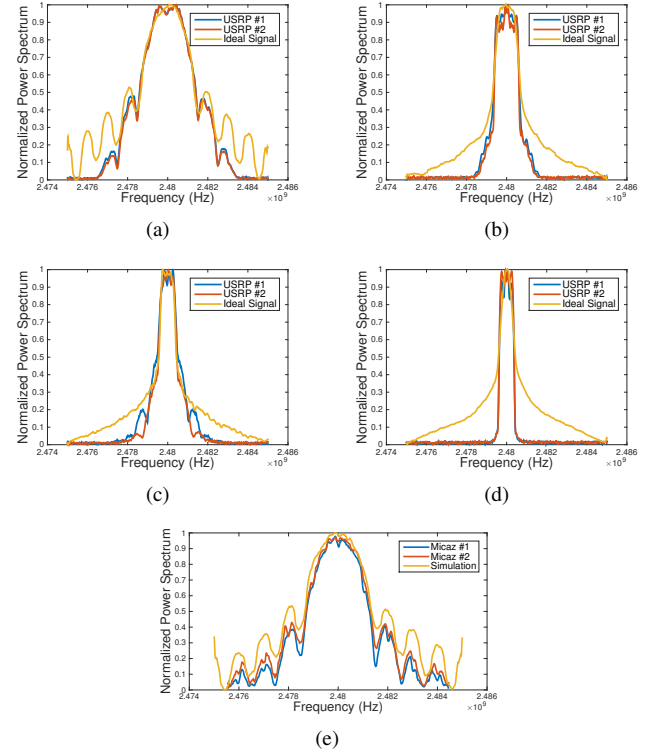


Fig. 3. PSDs of signals (a) using OQPSK and Half-sine Shaping (USRPs). (b) using OQPSK and RRC Shaping (USRPs). (c) using 8PSK and RRC Shaping (USRPs). (d) using 16QAM and RRC Shaping (USRPs). (e) using OQPSK and Half-sine Shaping (MicaZ).

eliminates the leakage and harmonics of the side lobes. From the perspective of the communication regulation, RRC shaping filter definitely performs better in terms of eliminating the interference to other wireless service in the adjacent frequency band. However, since the RFF considered in this paper shows more uniqueness in the spectrum side lobes, the RRC also reduce the effectiveness of the RFF.

Similar effects are shown in different modulation schemes. Fig. 3(c) and Fig. 3(d) compare the PSDs using 8PSK and 16QAM modulation schemes. As the modulation order increases, the signal power is more restricted in the main lobes and the RFF uniqueness is only observable in the small bandwidth of the main lobes. Besides the USRPs, we also take the non-linear system coefficient sets ( $\tilde{\mathbf{a}}_{\text{tx}}$ ) from the measurements of two MicaZ sensors (OQPSK modulation and half-sine shaping filter), which show more obvious nonlinear distortions. In Fig. 3(e), the PSDs of the two sensors are shown accompanying with the ideal signal without fingerprinting distortions. The results confirm that the RFFs due to non-linear front-end amplifier are more significant in the side lobes of the signal spectrum.

### C. Wireless Multipath Channel: Impact of Practical Environments

As discussed in Section II-B, the complex multipath channel can dramatically change the effectiveness of RFFs from the transmitter. While the ray-tracing model given in (6) is very accurate, it lacks the theoretical insights and cannot be further abstracted. Hence, in this subsection, we utilize the widely used statistical multipath channel models, including the

AWGN channel, Rayleigh channel, Rician channel, and Nakagami channel, to analyze the channel impacts. The Rayleigh model is frequently used to model multipath fading with no direct line-of-sight path. The Rician model is often used when there is one strong direct line-of-sight component and many random weaker components. The Nakagami- $m$  model gives the best fit to land mobile and indoor-mobile multipath propagation. As the parameter  $m$  increases to infinite, the Nakagami- $m$  channel converges to a AWGN channel. We consider the signal bandwidth is smaller than the channel coherent bandwidth [30]. As a result, the channel effects on spectrum fingerprints can be considered as a flat spectrum amplitude fading, which consists of a large scale path loss  $\alpha_{pl}$  and small scale multipath fading  $\alpha_{ch}$  [31]. Then the intensity of the EM waves at the RX antenna can be simplified as

$$\vec{A}_{rx}(t) = \vec{A}_{tx}(t) \cdot \alpha_{pl} \cdot \alpha_{ch} + N_{AWGN} \quad (22)$$

where  $N_{AWGN}$  is the channel background noise; the large scale path loss  $\alpha_{pl}$  in logarithm scale at distance  $d$  is given by

$$\alpha_{pl}[dB] = \alpha_{pl}(d_0) - 10\eta \cdot \log\left(\frac{d}{d_0}\right) \quad (23)$$

where  $\alpha_{pl}(d_0)$  is the path loss at the reference distance  $d_0$ ,  $\eta$  is the path loss exponent,  $X_{\sigma}$  is a normal random variable.

For the small scale channel effects, while the AWGN channel simply has the  $\alpha_{ch} = 1$ , the probability density function (PDF) of  $\alpha_{ch}$  in Rayleigh, Rician, and Nakagami- $m$  channel are [30]:

$$\begin{aligned} p_{Ray}(\alpha) &= \frac{2\alpha}{\Omega} \exp\left(-\frac{\alpha^2}{\Omega}\right) \quad (24) \\ p_{Nak}(\alpha) &= \frac{2m^m \alpha^{2m-1}}{\Omega^m \Gamma(m)} \exp\left(-\frac{m\alpha^2}{\Omega}\right) \\ p_{Ric}(\alpha) &= \frac{2(1+n^2)e^{-n^2\alpha}}{\Omega} \exp\left[-\frac{(1+n^2)\alpha^2}{\Omega}\right] I_0\left(2n\alpha \sqrt{\frac{1+n^2}{\Omega}}\right) \end{aligned}$$

where  $\alpha$  is channel fading amplitude with mean-square  $\Omega = \alpha^2$ ;  $m$  is the Nakagami- $m$  fading parameters which ranges from  $\frac{1}{2}$  to  $\infty$ ; where  $n$  is the Nakagami- $n$  fading parameter is related to the Rician  $K$  factor by  $K = n^2$ ;  $I_0(\cdot)$  is the zeroth-order modified Bessel function of the first kind.

By applying the above channel effects on the PSDs of the radiated signal at the transmitter, Fig. 4(a) show how the signal PSD changes along a Rayleigh multipath channel. The red curve is the signal PSD at 0.1m away from the transmitter while the blue curve is the PSD 6m away from the transmitter. A very significant distortion can be observed due to the wireless channel effect. Fig. 4(b) shows the PSDs of the two MicaZ sensors 6m away from the transmitters. Compared with the PSD of the same sensors in Fig. 3(e) when the distance is 0m, we find that the side lobes of the PSDs (where the most identity information resides) are mostly ruined by channel effects. That is the reason why most WPLI systems need to update the identifiers' fingerprint database and threshold whenever the user moves or the channel condition changes. It also explains why the WPLI performance are poor over the multipath channel.

#### D. Sampling and FFT: Influence of Receiver Device

As modeled in Section II-C, the receiver captures/processes the wireless signal and finally derives the sampled digital signals  $\{x[n]\}$ . Since the WPLI technique considered in this

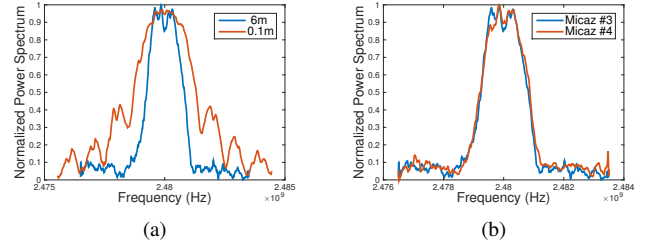


Fig. 4. (a) PSDs of RFF-stamped signals at different distance. (b) PSDs of RFF-stamped signals from two devices at 6 m.

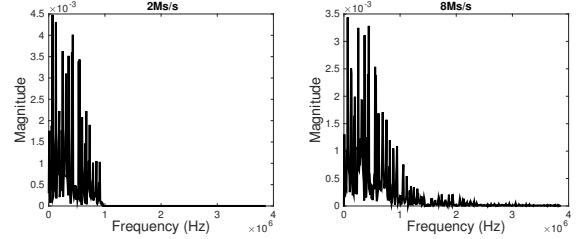


Fig. 5. FFT PSDs with different sampling rate.

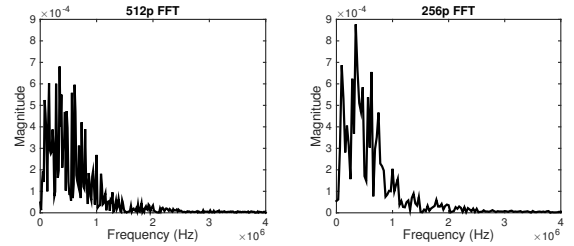


Fig. 6. FFT PSDs (8Ms/s) with different number of FFT points.

section requires the frequency domain feature, the fast Fourier transform (FFT) is applied to the sampled digital signals, which is actually part of the feature extraction modeled in (12). The output of the  $N_{FFT}$ -points FFT transformation is:

$$X[k] = \sum_{n=0}^{N_{FFT}-1} x[n] \cdot e^{-2\pi i k n / N_{FFT}} \quad (25)$$

where  $f_s = 1/T_s$  is the ADC sampling rate. The ADC sampling rate  $f_s$  as well as the bandwidth of the LPF in (10) determine the bandwidth of the FFT spectrum. The FFT point number  $N_{FFT}$  controls the frequency domain resolution. According to the FFT properties,  $N_{FFT} \geq L$ , where  $L$  is the length of the sampled signal. In most WPLI systems,  $N_{FFT}$  is fixed to the length of the tested data (e.g., the signal preamble [18]).

The effects of different receiver sampling rates are illustrated in Fig. 5, where the FFT spectrum from one of the MicaZ sensors in Fig. 4(b) are plotted with two different sampling rates. We observe that the higher sampling rate keeps more RFF identification information that mainly resides in the side lobes of the signal PSD. However, it should be also noted that the high sampling rate may also increase the noise band. If the SNR become very low in a long distance fading channel, the high sampling rate may not be a favorable option. Existing work keeps SNR high when the high-end measurement equipments are used. In the Fig. 6, the FFT PSDs of the same signal with different FFT points are shown. It is clear that the higher FFT point number increases the frequency domain resolution. However, we don't find clear relationships between the higher FFT resolution with the better identification performance. Part

of the reason is that we always keep  $N_{FFT}$  larger than the length of sampled signal in time domain.

### E. Error Rate in Classification & Identification: Final Metrics

Although the above analysis gives qualitative explanation on the real-world constraints and requirements of WPLI systems, the quantitative evaluation needs the error rates in classification or identification as the final metrics, which is theoretically derived in this subsection. Before calculating the error rates, the RFF needs to be extracted and compared with the reference RFFs.

1) *Fingerprint Extraction*: As discussed at the beginning of this section, the only RFF considered in this WPLI system is the TX RF front-end non-linearity. The other hardware imperfections are considered as additional noises on top of ideal circuit while the multipath channel effects are considered as random process defined by the statistical channel models. Hence, we can rewrite the FFT result of the sampled digital signal  $X[k]$  as a function of the TX baseband signal  $u(t)$ :

$$\mathbf{X} = \alpha_{pl} \cdot \alpha_{ch} \cdot \tilde{\mathbf{U}} \cdot \mathbf{H}_{tx} \cdot \mathbf{H}_{tx}^T + \mathbf{N}; \quad (26)$$

where  $\mathbf{X}$  is the vector  $\{X[k], k = 1, 2, \dots\}$ ; the channel effect is represented by the path loss  $\alpha_{pl}$ , the fading  $\alpha_{ch}$ , and the background noise (part of  $\mathbf{N}$ ), as modeled in (22); the RF front-end non-linearity at transmitter is characterized by  $\mathbf{H}_{tx}$ , which is determined by the a unique coefficient set  $\tilde{\mathbf{a}}_{tx} = \{a_n\}$  of the non-linear system at the TX RF front-end described in (21), in particular:

$$\mathbf{H}_{tx} = \begin{bmatrix} |\tilde{a}_1|^2 & \dots & \frac{\tilde{a}_{2n+1}\tilde{a}_{2m+1}^*}{2^{2(n+m)}} \binom{2n+1}{n+1} \binom{2m+1}{m+1} \end{bmatrix}^T.$$

Similarly,  $\mathbf{H}_{rx}$  in (26) describes the non-linearity at the receiver front-end but is considered as a known vector by the identifier. The receiver can cancel the effect of the non-linearity at the receiver front-end before the identification or classification. The influences of all the other hardware imperfections (clock circuit, DAC, and mixer) contribute to the other part of the additive noise  $\mathbf{N}$ . In (26), the TX baseband signal input is represented by a diagonal matrix  $\tilde{\mathbf{U}}$ :

$$\tilde{\mathbf{U}} = \text{Diag} \{ \tilde{U}_{11} \quad \dots \quad \tilde{U}_{2n+1,2m+1} \};$$

where  $\tilde{U}_{2n+1,2m+1}$  has the same formulation as the passband autocorrelation spectrum  $\tilde{S}_{(2n+1)(2m+1)}$  given in (21); the only difference is that the passband input  $z(t)$  is replaced with the baseband input  $u(t)$ .

In practical identification system, the signal receiver has the same effects on all the obtained fingerprints. However, between different receivers, the effects of RF front-end are different. The nonlinear series of receiver can be estimated, measured and corrected. In [32], [33], [27], the theoretical models of nonlinear series are proposed and approximate expression are presented, which can be utilized to estimate the receiver's nonlinear series. In [32], the experimental approach to measure the nonlinear series using vector signal generator and oscilloscope is also given. With obtained nonlinear series of receiver, the spectral regrowth of the signal due to receiver can be compensated using various algorithms [34], [35], [36].

After canceling the known influence of the RX front-end non-linearity, the sampled digital signal  $\mathbf{X}$  become the fingerprint at the receiver  $\mathbf{S}$ :

$$\mathbf{S} = \mathbf{X} \cdot \mathbf{H}_{rx}^T{}^{-1} = \alpha_{pl} \cdot \alpha_{ch} \cdot \tilde{\mathbf{U}} \cdot \mathbf{H}_{tx} + \tilde{\mathbf{N}} \quad (27)$$

We approximately modeled  $\tilde{\mathbf{N}}$  as a Gaussian noise since many independent sources jointly contribute to it.

The reference fingerprints of the authorized users in the database at the identifier  $\mathbf{S}_R$  can be expressed by

$$\mathbf{S}_R = \alpha_{pl,R} \cdot \alpha_{ch,R} \cdot \tilde{\mathbf{U}} \cdot \mathbf{H}_{tx,R}; \quad (28)$$

where  $\alpha_{pl,R}$  and  $\alpha_{ch,R}$  usually do not take effect since the reference fingerprints are obtained when the transmitter is very close to the receiver; all reference and device to be identified use the same transmitted signal packet so that they share the same known  $\tilde{\mathbf{U}}$ ; and  $\mathbf{H}_{tx,R}$  is the source of the fingerprints of the reference.

2) *Fingerprint Matching*: There are multiple ways to calculate the distance between the testing fingerprint  $\mathbf{S}$  with the reference fingerprint  $\mathbf{S}_R$ . The most straightforward way is to calculate the norm of the difference of the two vectors, i.e.,  $D(\mathbf{S}) = \|\mathbf{S} - \mathbf{S}_R\|$ . However, this method treats the difference of each frequency point equally and adds them together. In contrast, as we show in Fig. 3(a)-Fig. 3(e), the uniqueness of the RFFs shows more significant difference at the higher frequency range of the baseband signal. Hence, a more efficient way is to assign higher weight to the frequency points where the uniqueness of the RFFs is more obvious. To this end, the Linear Discriminant Analyses (LDA) strategy is introduced [37], [15], which assigns different weights to different frequency points according to the information from fingerprint database.

Consistency with the previous discussion, the covered bandwidth of the extracted fingerprint vector is determined by the receiver sampling rate, i.e.,  $BW = f_s/2$ . The length of the fingerprint vector is determined by the FFT points i.e.  $L_N = N_{FFT}$ . The prerequisite of effective LDA is that the receiver sampling rate is high enough to keep the majority of the fingerprint information and the FFT point number is larger than the data/preamble length. Under the LDA scheme, the feature distance  $D_i(\mathbf{S})$  between the incoming feature vector  $\mathbf{S}$  and the  $i^{th}$  reference feature vector  $\mathbf{S}_R^i$  is given by [37]:

$$D_i(\mathbf{S}) = \frac{\|\mathbf{W}_{LDA}^T \cdot (\mathbf{S} - \mathbf{S}_R^i)\|}{\sigma(\mathbf{W}_{LDA}^T \cdot \mathbf{S}_R^i)}, \quad (29)$$

where  $\mathbf{W}_{LDA}$  is the LDA feature matrix that is derived based on the fingerprint database of the authorized users;  $(\cdot)^T$  indicate the matrix transpose;  $\sigma(\cdot)$  is the standard deviation function of a vector. We do not elaborate the procedures in training the LDA feature matrix. Detailed formulas can be found in [37].

3) *Classification Error Rate*: In device classification, the testing feature vector  $\mathbf{S}$  is matched to all the reference fingerprints  $\{\mathbf{S}_R^i, i = 1, 2, \dots\}$  and assigned to the identity with the smallest distance score. Then the classification decision probability  $P(\mathcal{H}_i|\mathcal{H}_j)$  can be calculated according to (14). Without loss of generality, we consider a two-user scenario to derive the classification probabilities.

The two class classification scenario is between two genuine user,  $\mathcal{H}_1$  and  $\mathcal{H}_2$ . The feature distance from the incoming vector to the two reference vectors are  $D_1$  and  $D_2$ . Then the classification decision rule becomes  $D_\Delta \stackrel{def}{=} D_1 - D_2 \underset{\mathcal{H}_1}{\underset{\mathcal{H}_2}{\geq}} 0$ . Then the average classification error rate can be derived:

$$P_e = P(D_\Delta > 0|\mathcal{H}_1)P(\mathcal{H}_1) + P(D_\Delta < 0|\mathcal{H}_2)P(\mathcal{H}_2); \quad (30)$$

where we can safely assume  $P(\mathcal{H}_1) = P(\mathcal{H}_2) = 0.5$ ; and

$$P(D_\Delta > 0|\mathcal{H}_1) = \int_{\frac{\sigma_{G_R^2}^2 s_R^1 - \sigma_{G_R^1}^2 s_R^2}{\sigma_{G_R^2}^2 - \sigma_{G_R^1}^2}}^{\sigma_{G_R^2}^2} \frac{\|W\|(\sigma_{G_R^2}^2 - \sigma_{G_R^1}^2)}{\sigma_{G_R^1}^2 \sigma_{G_R^2}^2} p(\mathbf{S}|\mathcal{H}_1) d\mathbf{S}. \quad (31)$$

Note that  $P(D_\Delta < 0|\mathcal{H}_2)$  can be derived in the same way.

In order to compute  $p(\mathbf{S}|\mathcal{H}_i)$ , we define  $\mathbf{L} \stackrel{def}{=} \alpha_{pl} \alpha_{ch} \cdot \tilde{\mathbf{U}} \cdot \mathbf{H}_{\mathbf{t}\mathbf{x}}$  so that  $\mathbf{S} = \mathbf{L} + \tilde{\mathbf{N}}$  according to (27). Then, the conditional probability density  $p(\mathbf{S}|\mathcal{H}_i)$  can be derived by

$$p(\mathbf{S}|\mathcal{H}_i) = \int_{-\infty}^{+\infty} p_L(\mathbf{x}|\mathcal{H}_i) p_{\tilde{\mathbf{N}}}(\mathbf{S} - \mathbf{x}) d\mathbf{x}; \quad (32)$$

where  $p_{\tilde{\mathbf{N}}}$  is the probability density of a zero-mean Gaussian variable with a predetermined variance;  $p_L(\mathbf{x}|\mathcal{H}_i)$  is determined by the statistical channel models given in (24):

$$p_L^{Ray}(\mathbf{L}|\mathcal{H}_i) = \frac{2\|(\alpha_{pl}^{-1} \tilde{\mathbf{U}}^{-1} \mathbf{L} \mathbf{H}_{\mathbf{t}\mathbf{x}}^i)^{-1}\|}{\Omega} \cdot e^{-\frac{\|(\alpha_{pl}^{-1} \tilde{\mathbf{U}}^{-1} \mathbf{L} \mathbf{H}_{\mathbf{t}\mathbf{x}}^i)^{-1}\|^2}{\Omega}} \quad (33)$$

$$p_L^{Nak}(\mathbf{L}|\mathcal{H}_i) = \frac{2m^m (\|\alpha_{pl}^{-1} \tilde{\mathbf{U}}^{-1} \mathbf{L} \mathbf{H}_{\mathbf{t}\mathbf{x}}^i\|)^{2m-1}}{\Omega^m \Gamma(m)} \cdot e^{-\frac{m(\|\alpha_{pl}^{-1} \tilde{\mathbf{U}}^{-1} \mathbf{L} \mathbf{H}_{\mathbf{t}\mathbf{x}}^i\|)^2}{\Omega}}$$

$$p_L^{Ric}(\mathbf{L}|\mathcal{H}_i) = \frac{2(1+n^2)e^{-n^2} (\|\alpha_{pl}^{-1} \tilde{\mathbf{U}}^{-1} \mathbf{L} \mathbf{H}_{\mathbf{t}\mathbf{x}}^i\|)}{\Omega} \cdot e^{-\frac{(1+n^2)(\|\alpha_{pl}^{-1} \tilde{\mathbf{U}}^{-1} \mathbf{L} \mathbf{H}_{\mathbf{t}\mathbf{x}}^i\|)^2}{\Omega}} \cdot I_0 \left( 2n(\|\alpha_{pl}^{-1} \tilde{\mathbf{U}}^{-1} \mathbf{L} \mathbf{H}_{\mathbf{t}\mathbf{x}}^i\|) \sqrt{\frac{1+n^2}{\Omega}} \right)$$

Note that the AWGN channel does not have multipath fading. Hence,  $\mathbf{S}$  becomes a Gaussian variable with the same variance but different mean values, whose condition probability can be easily derived.

4) *Numerical results of classification:* Based on (30)-(33), we can numerically evaluate the classification error rate in different channels (AWGN, Rayleigh, Nakagami  $m = 3$ , Rician  $K = 4$ ) and with different receiver sampling rate (2M-8MHz). When different channel/distance is considered, we need to first determine the strategy on how to build the fingerprint database. On the one hand, in most existing work [15], the fingerprint database is updated with the new channel characteristics whenever the transmitter or receiver change location. On the other hand, we believe the frequent database update is not feasible in many wireless applications. Hence, we evaluate both strategies. Fig. 7 shows the classification error rate of different channel as a function of distance. The fingerprint database is updated at each point along the curves. Even with this infeasible strategy, we observe that the error rate increases dramatically if the transmission distance increases or the multipath channel is involved. Due to the lack of line-of-sight path, the Rayleigh channel gives the worse performance while the more friendly AWGN channel has the best performance. In Fig. 8, we fix the reference fingerprint (measured at the very close distance, 0.1 m) and

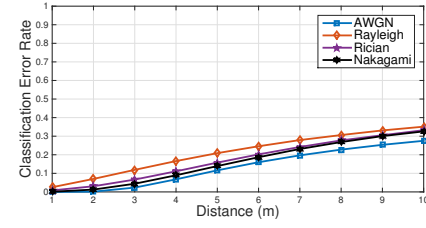


Fig. 7. Classification error rates over different channels with updated database.

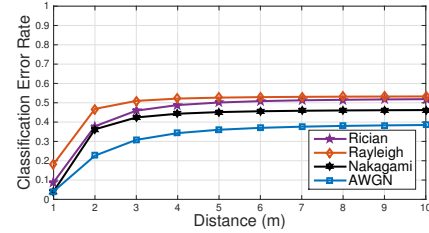


Fig. 8. Classification error rates over different channels with fixed database.

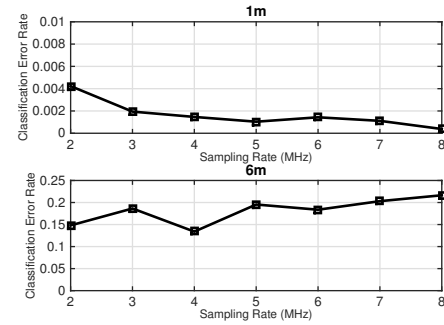


Fig. 9. Classification error rates with different receiver sampling rates.

plot error curves at different distances over different channels. We observe very poor classification performance. The error rate approach 50% (i.e., loss of classification capability) within 10 m in the Rayleigh channel.

Besides the channel effect, we also evaluate the influence of the receiver sampling rate on the classification error rates. In Fig. 9, the numerical results of average classification rates due to different sampling rate are shown. To avoid the multipath effects and also to show the trade off in sampling rates, we calculate the numerical results at 1m and 6m under AWGN channel. At the close distance, where the SNR level of the channel is high (25dB), the classification error rate decreases with the increasing of sampling rate. This is because more side-lobe information of spectrum are covered by the fingerprinting sampling bandwidth. At 6m distance, the classification performance become worse in higher sampling rate situation. The reason for this phenomena is that most side-lobe information are ruined by increased noise band when the channel SNR level is low (15dB). At some sampling rate points the more signal information involved than the noise and at other points more noise are involved. Hence the choice of the sampling rate is the trade off between the different application scenarios due to the analyses in the previous section.

5) *Identification Error Rate:* Different from the classification, authorized user/imposter detection can be considered as a two-user hypothesis model. Due to the lack of knowledge

on imposters' fingerprints, we cannot know which frequency point carries more significant identification information. As a result, the LDA scheme assigns the same weights for all frequency points of the feature vectors. Then the identification simply relies on the direct difference between the incoming feature vector and the reference vector  $\mathbf{d} = \mathbf{S} - \mathbf{S}_R^1$ . As previously defined,  $\mathcal{H}_1$  denotes the authorized users while  $\mathcal{H}_0$  denotes imposters. According to the decision rule in (16), the judging threshold  $\lambda$  needs to be determined first by finding the operational point in the ROC chart. In most existing work,  $\lambda$  is updated whenever the fingerprint database of authorized users is updated. However, we can also change the strategy by fixing the database and threshold after the first update. The difference between the incoming feature and the reference under  $\mathcal{H}_1$  can be deduced as

$$\mathbf{d}|\mathcal{H}_1 = \mathbf{S}_1 - \mathbf{S}_R^1 = \tilde{\mathbf{N}} \quad (34)$$

Similarly,

$$\begin{aligned} \mathbf{d}|\mathcal{H}_0 &= \mathbf{S}_0 - \mathbf{S}_R \\ &= (\alpha_{pl,0} \cdot \alpha_{ch,0} \cdot \tilde{\mathbf{U}} \cdot \mathbf{H}_{un} - \alpha_{pl,1} \cdot \alpha_{ch,1} \cdot \tilde{\mathbf{U}} \cdot \mathbf{H}_{ix}) + \tilde{\mathbf{N}} \end{aligned} \quad (35)$$

where  $\mathbf{H}_{un}$  is RF front-end series of the imposter (unknown to identifier). According to (34) and (35), the identification problem can be simplified as a signal detection problem:  $\mathcal{H}_1$  indicates that the difference vector  $\mathbf{d}$  is a zero-mean Gaussian noise; while  $\mathcal{H}_0$  indicates that  $\mathbf{d}$  is a signal under the influence of the multipath fading channel and the Gaussian noise. Then we can apply the classical energy detection model [38] that detects unknown signal over fading channels. In AWGN channels, the identification GRR can be calculated by

$$P_{AWGN}(\mathcal{H}_0|\mathcal{H}_0) = Q_\mu(\sqrt{2\gamma}, \sqrt{\lambda}), \quad (36)$$

where  $Q_\mu(\cdot)$  is the generalized Marcum Q-function,  $\gamma$  is the SNR of difference vector  $\mathbf{d}$  over the Gaussian noise  $\tilde{\mathbf{N}}$ ; and  $\lambda$  is the judging threshold. In Rayleigh channels, the identification GRR is

$$\begin{aligned} P(\mathcal{H}_0|\mathcal{H}_0)_{Ray} &= e^{-\frac{\lambda}{2}} \sum_{n=0}^{\mu-2} \frac{1}{n!} \left(\frac{\lambda}{2}\right)^n \\ &+ \left(\frac{1+\gamma}{\gamma}\right)^{\mu-1} \left[ e^{-\frac{\lambda}{2(1+\gamma)}} - e^{-\frac{\lambda}{2}} e^{-\frac{\lambda}{2}} \sum_{n=0}^{\mu-2} \frac{1}{n!} \frac{\lambda\gamma}{2(1+\gamma)} \right], \end{aligned} \quad (37)$$

where  $\mu$  is the time bandwidth product. And in Nakagami-m channels, identification GRR is:

$$P(\mathcal{H}_0|\mathcal{H}_0)_{Nak} = \alpha \left[ G_1 + \beta \sum_{n=1}^{\mu-1} \frac{(\lambda/2)^n}{2(n!)} {}_1F_1(m; n+1; \frac{\lambda}{2} \frac{\gamma}{m+\gamma}) \right] \quad (38)$$

where  $m$  is the Nakagami-m parameter;  ${}_1F_1(\dots)$  is the confluent hypergeometric function;  $\alpha$  and  $G_1$  are parts of the equations which can be find in the specific form in [38]. Finally, in Rician channels, GRR is given by

$$P(\mathcal{H}_0|\mathcal{H}_0)_{Ric} = Q\left(\sqrt{\frac{2K\gamma}{K+1+\gamma}}, \sqrt{\frac{\lambda(K+1)}{K+1+\gamma}}\right), \quad (39)$$

where  $K$  is the Rician factor;  $Q(\cdot) = Q_1(\cdot)$  is the first-order Marcum Q-function.

For all the four types of channels (AWGN, Rayleigh, Nakagami, and Rician), the FRR remains the same, which is

$$P(\mathcal{H}_0|\mathcal{H}_1) = \frac{\Gamma(\mu, \frac{\lambda}{2})}{\Gamma(\mu)}. \quad (40)$$

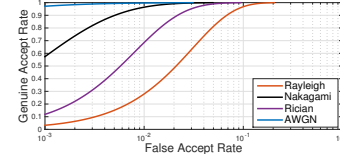


Fig. 10. Theoretical ROC curves over different channels.

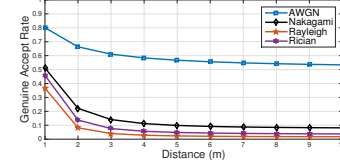


Fig. 11. Genuine Accept Rate over different channels (with fixed database).

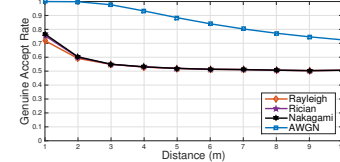


Fig. 12. Genuine Accept Rate over different channels (with updated database).

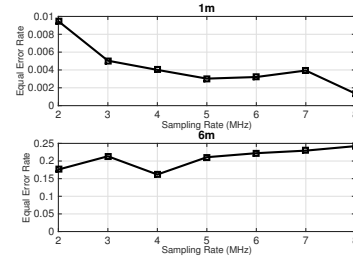


Fig. 13. Equal Error Rates with different receiver sampling rates.

where  $\Gamma(\cdot)$  is the incomplete gamma function.

It should be noted that the GRRs and FRRs given in (36)-(40) are all functions of the SNR  $\gamma$ . Here the SNR is not the ratio of the total signal over noise but the ratio of feature difference over noise. To use this theoretical tool, system designers firstly traverse the possible threshold to calculate the theoretical identification error rate for certain  $\gamma$ . Then the results of identification error rates can be drawn into the ROC charts. According to ROC charts of different SNR scenarios are drawn, the system designers can have a clear understanding of the performance of WPLI in the targeted application scenario. Hence, the proper threshold can be selected as the operational point. Moreover, since the feature of imposters is unknown, higher receiver sampling rate can help increase  $\gamma$  by involving more possible significant device differences in a wider spectrum, if the overall noise level is low. However, if the noise level is high, higher receiver sampling rate may reduce  $\gamma$  and harm the identification performance.

6) *Numerical results of identification:* Based on the derived model, we calculate the theoretical error rate to evaluate the influence of the wireless channel and receiver sampling rate. Similar to the settings in the classifications, we derive the authorized user's fingerprint and judging threshold at a very close distance (0.1m). Fig. 10 shows the ROC curves of different channel types at the distance of 0.1 m. Then we choose the EER point (0.1%) on the AWGN curve as the judging threshold. In Fig. 11, we fix the threshold and reference fingerprints. The identification GARRs at different

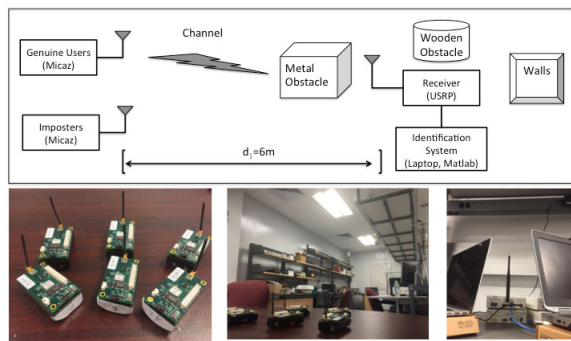


Fig. 14. Experimental setup.

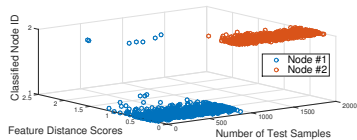


Fig. 23. Classification results at 3m, 1024p FFT

distance over different channels are plotted. We observe that if the reference fingerprint and threshold are fixed, the identification performance dramatically deteriorates as the transmission distance increases or the multipath channel model is applied. In contrast, Fig. 12 shows the identification GARs when the reference database and judging threshold get updates at each plot point. Obvious performance improvements are observed but the influence of longer transmission distance and the multipath channel is still significant.

In Fig. 13, the numerical results of equal error rate due to different sampling rate are shown. Similarly, we calculate the numerical results at 1m and 6m under AWGN channel. At the close distance, the equal error rate decreases with the increasing of sampling rate. However, at longer distance, the performance of identification become worse with the increasing of sampling rate. Hence the choice of the sampling rate is still a trade off for identification performance under different application scenarios.

#### IV. EXPERIMENTAL ANALYSIS

In this section, we experimentally validate the real-world constraints of WPLI analyzed in Section III. The experimental setup and scenarios are first described. Then the influence of wireless channels, receiver sampling rates, and FFT points on the identification and classification performance of WPLI are analyzed through a series of experiments.

##### A. Experimental Setup and Scenarios

The experimental setup is illustrated in Fig. 14. The transmitters (device to be identified) are 6 Micaz sensors nodes, which is a IEEE 802.15.4 compliant RF transceiver with the RF frequency band ranging from 2.4 to 2.48 GHz [28]. The modulation scheme and shaping filter used in IEEE 802.15.4 protocol are fixed, which are O-QPSK with half-sine pulse shaping filter [39]. The baseband transmitting symbol rate 1 M symbol per second. The data packet preamble is used to extract the RFF, which has a length of 32 bits all-zero data (128 symbols for either I/Q-phase signal after modulation and spread spectrum procedure). All the sensor nodes are powered

by AA batteries of a same brand, which are also changed with new ones for each time of data collection. More than 10,000 data packets are captured for each transmitter to obtain reliable results. We use USRP N210 companied with SBX daughter board [29] as the receiver (identifier).

The receiver is either 1 m, 3 m, or 6 m away from the transmitters to obtain the large scale attenuation effects. Meanwhile, the receiver is placed in the middle of a circle of the metal obstacles (laptops), wooden obstacles (book shelves), and the concrete wall, as shown in Fig. 14. Hence, no direct line-of-sight wireless link exists and obvious multipath effects can be observed. In the experiments to validate the effects of receiver sampling rates and FFT points, we place the receiver in an in-door open space to build an AWGN-type channel so that the receiver’s settings take major effects (other than the multipath channel). A laptop with MATLAB 2014b is connected to the USRP receiver. The packet preambles are extracted from data files obtained in USRP and the LDA-based identification and classification algorithms are realized in MATLAB. To extract the preambles from the data files, the variance-based threshold detection algorithm [40] is adopted. The LDA dimension  $\kappa = 5$  is fixed in all experiments.

In order to analyze the influence from wireless channels, we first build fingerprint database and obtain identification threshold at very small distance (0.1 m). The classification/identification performance is also obtained as the best case for comparison. Then we place the transmitter and receiver in the aforementioned multipath fading channel and conduct the experiment in three scenarios. In the first scenario, we update the reference database and identification threshold at each new location, which is the common strategy that existing work adopt. In the second scenario, we do not update the reference database and check the classification/identification results. The objective of this scenario is to validate whether the existing WPLI systems with a universal fingerprint database and threshold can work with mobile users or in dynamic channels. Moreover In the third scenario, we do not update the reference database but normalize the test samples from different channels and distances. The purpose is to check whether the large scale path loss is the main source of the channel effects and whether the normalization can eliminate the influence from channels.

In order to analyze the influence from the receiver sampling rate, we set two different sampling rates (i.e., 2 Ms/s and 8 Ms/s) in USRP. Fixed spectrum resolution is used when building the fingerprints database and extract fingerprints from incoming signal. The 2 Ms/s sampling rate can only cover the main lobes of the spectrum while the 8 Ms/s can recover more side lobe information, as shown in Fig. 5. Whether the sampling rate effectively covers enough bandwidth is determined by both the hardware of the receiver and the modulation/shaping filter of the transmitter. Since the MicaZ sensors have fixed modulation scheme and shaping filter, the receiver sampling rate plays major role in our experiments. In order to check the effects of FFT point number at the receiver, the same data file is obtained with a single sampling rate in USRP receiver. However, we use the different FFT point number in feature extraction to realize the fingerprints with

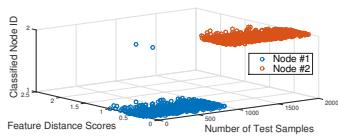


Fig. 15. Classification results at 0.1m

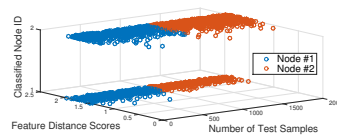


Fig. 16. Classification results at 6m with fixed database.

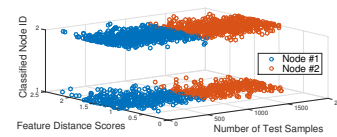


Fig. 17. Classification results at 6m without large scale path loss effects.

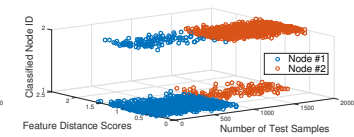


Fig. 18. Classification results at 6m with updated database

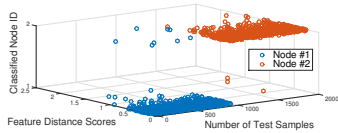


Fig. 19. Classification results at 1m, 2Ms/s

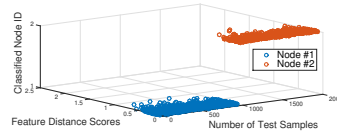


Fig. 20. Classification results at 1m, 8Ms/s

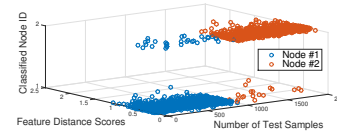


Fig. 21. Classification results at 3m, 256p FFT

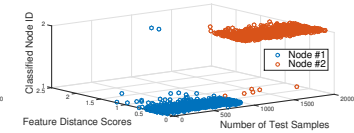


Fig. 22. Classification results at 3m, 512p FFT

the same signal bandwidth but different spectrum resolution, as shown in Fig. 6.

### B. Classification Performance

In this group of the experiments, the classification performance are tested to capture the effects of channel, database updating strategy, sampling rates, and FFT point number. The sensor node #1 and #2 are used as the two genuine users to be classified. In Fig. 15 - Fig. 23, the x-axis is the index of the test samples. The first 1000 are samples from Node #1 and the next 1000 are from Node #2. The y-axis is the minimal feature distance of each test sample. The color of each testing sample indicates the original identity of the signal: blue - Node #1 and red - Node #2. The z-axis is the classification results: there is a classification error if blue circles appear in upper level or red circles appear in lower level.

1) *Initialization:* We start the roll in and the classification at the close distance (0.1m,  $f_s = 4Ms/s$ ,  $N_{FFT} = 512$ ). According to the results shown in Fig. 15, the classification performance is exceptional where only two samples are wrongly classified, i.e., the average classification error rate  $P_e = 0.001$ .

2) *Channel effects:* We place the receiver in the aforementioned non-line-of-sight multipath channel at 6 m away from transmitter. At first, we do not update the reference database. The results are shown in Fig. 16 where the classification error rate  $P_e = 0.4910$ , i.e., complete loss of classification capability.

Then in order to check whether the attenuation over distance (i.e., path loss) is the main impact on the performance, we eliminate the path loss effects by normalizing the test samples and redo the classification. The results are shown in Fig. 17 where  $P_e = 0.4830$ . The feature distance scores are smaller but the classification performance is as poor as before. Hence, we can conclude that path loss is not the main source of the channel effects and the sample normalization cannot mitigate the impact.

Finally, we adopt the existing approach to update the reference database at the new location before classification. The results are shown in Fig. 18 where  $P_e = 0.1388$ . It is obvious that the system resume part of the classification capability if the less practical database updating strategy is used. However, compared with the results at the close distance, the performance is much worse due to the multipath channel. It should be noted that the real indoor or metropolitan channel

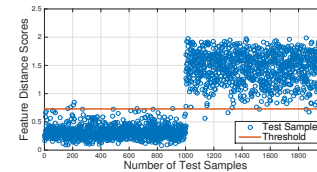


Fig. 32. Identification results at 3m, 1024p FFT.

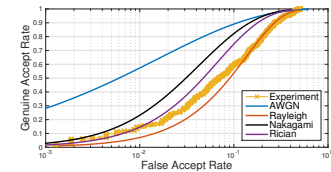


Fig. 33. Experimental and theoretical ROC curves.

can be much worse and hostile than the short-range artificial multipath channel we build in our experiments.

3) *Effects of sampling rate:* Due to property of USRP hardware, the bandwidth of its half-band filter are set to be  $W = f_s/2$ . Hence the fingerprint bandwidth  $BW$  equals to the receiver bandwidth  $W$ . The classification results can be influenced by both the two factors. We set the sampling rate as either  $f_s = 2Ms/s$  or  $f_s = 8Ms/s$ . To make sure the receiver effects are not merged by the channel effects, we put the receiver only 1 m away from the transmitter and there is no obstructions in between. To achieve the same spectrum fingerprinting resolution,  $N_{FFT} = 256$  when  $f_s = 2Ms/s$  and  $N_{FFT} = 1024$  when  $f_s = 8Ms/s$ . The classification results are shown in Fig. 19 and Fig. 20, where the classification error rates are  $P_e = 0.0055$  and  $P_e = 0$ , respectively. As the previous analyses, at high SNR scenarios, like the close distance at 1m, the higher sampling rates can involve more side-lobe information. Hence, the higher sampling rate improves the performance by involving higher frequency spectrum where the RFF is still significant. However, high sampling rate can help only when the distance is short, the SNR is high, and the RFF indeed occupy the higher frequency band. If the transmission distance is large and the SNR is low, the non-significant RFF may be merged by noise. Increasing the sampling rate can introduce more noise if the extra fingerprinting spectrum has low SNR. Hence, the optimal sampling rate need to be determined by jointly consider the channel effects, the origin of the RFF, and the regulation of the modulation scheme and shaping filter.

4) *Effects of number of FFT points:* To test the effects of FFT point number, the receiver is again placed at a close distance at 3 m and the sampling rate is set as  $f_s = 8Ms/s$ . The classification results using  $N_{FFT} = 256$ ,  $N_{FFT} = 512$ , and  $N_{FFT} = 1024$  are shown in Fig. 21, Fig. 22, and Fig. 23, where the classification error rates are  $P_e = 0.0255$ ,

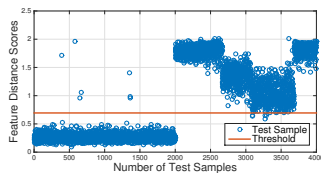


Fig. 24. Identification results at 0.1m.

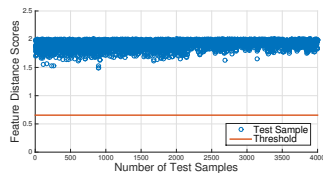


Fig. 25. Identification results at 6m, fixed database

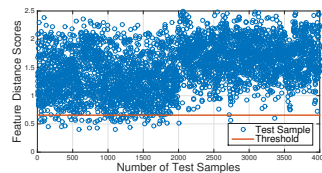


Fig. 26. Identification results at 6m, without large scale path loss.

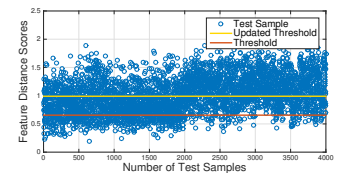


Fig. 27. Identification results at 6m, updated database.

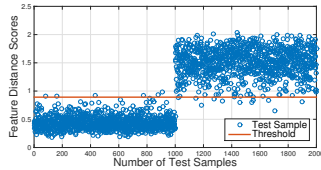


Fig. 28. Identification results at 1m, 2Ms/s.

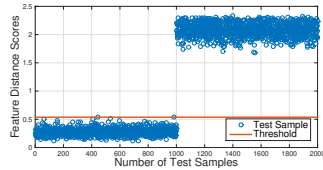


Fig. 29. Identification results at 1m, 8Ms/s.

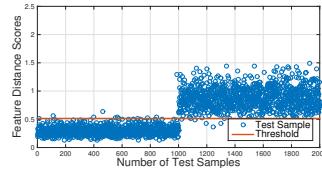


Fig. 30. Identification results at 3m, 256p FFT.

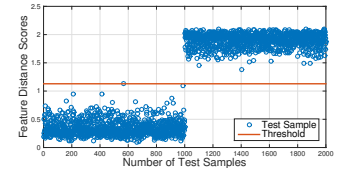


Fig. 31. Identification results at 3m, 512p FFT.

$P_e = 0.004$ , and  $P_e = 0.0035$ , respectively. The classification performance is improved with a large scale from 256p to 512p. There is no significant improvement on the performance with different FFT point number, if the spectral resolution is accurate enough, as between 512p and 1024p. Hence, there is no need to use ultra high FFT point number that add additional computation burden.

### C. Identification Performance

In this group of the experiments, the above influence factors are analyzed again but in the identification procedure. The sensor node #5 is used as the genuine user, while the nodes #1 #4 are used as the imposters. In Fig. 24 - Fig. 32, the x-axis is the index of the test samples. The first half of samples (1000 or 2000) are samples from genuine user #5. The rest of samples are from imposters. The y-axis is the feature distance score of each test sample. The horizontal red line is the judging threshold. The samples below the threshold are identified as genuine user, otherwise are identified as imposters.

1) *Initialization*: Similarly to the classification experiments, we start the roll in and the classification at the distance of 0.1 m in Fig. 24. After obtaining the feature distance scores of all the testing samples, we choose the point, where the equal error rate  $EER = 0.0030$  is achieved, as the judging threshold of the identification system, i.e.,  $\lambda_{EER} = 0.655$ .

2) *Channel effects*: Again, we place the receiver in the artificial non-line-of-sight multipath channel at 6 m away from transmitter. We fix the reference database and judging threshold. The results are shown in Fig. 25 where  $GAR = 0$  and  $FAR = 0$ . Similar to the classification case, the system completely lose the identification capability.

Then we eliminate the path loss effects by normalizing the test samples. The results are shown in Fig. 26 where  $FAR = 0.0010$  and  $GAR = 0.0305$ . The identification capability is still very weak. Hence, we can again conclude that the multipath channel impact cannot be mitigated by simply compensating the path loss.

Finally, we update the reference database and reset the threshold at every new location: not practical in most applications but the same as most existing WPLI solutions. The new results are shown in Fig. 27 where the threshold,  $\lambda_{EER} = 0.9900$ , is reset to achieve the  $EER = 0.3205$ .

However, the identification performance is still much worse than the case when distance is short, which is obviously caused by the effects of multipath channel. Fig. 33 shows the ROC curve derived in the experiment with the multipath channel and 6 m distance. The theoretical ROC curves under the same SNR level derived in Section III are also plotted for comparison. We can clearly see the experimental curve has the best match with the theoretical Rayleigh ROC curve, which is consistent with expectation in the non-line-of-sight multipath channel we build in our lab.

3) *Effects of sampling rate*: To focus on the effects of the sampling rate of the receiver, we only use two transmitters, i.e., genuine user - Node #5 and imposter - Node #4. 1000 samples are taken for each device that is 1 m away from each other. When lower sampling rate are used, i.e.,  $f_s = 2Ms/s, N_{FFT} = 256$ , the results are shown in Fig. 28 where  $EER = 0.008$  and  $\lambda_{EER} = 0.892$ . When higher sampling rate are used, i.e.,  $f_s = 8Ms/s, N_{FFT} = 1024$ , the results are shown in Fig. 29 where  $EER = 0$  and  $\lambda_{EER} = 0.537$ . The same comments as in the classification experiment also apply here.

4) *Effects of number of FFT points*: Finally, the identification results with different FFT point number are given in Fig. 30, Fig. 31, and Fig. 32. The data are collected at 3m, with 8 Ms/s sampling rate. The equal error rates and threshold for the each case are  $EER = 0.01, \lambda_{EER} = 0.5150$ ;  $EER = 0, \lambda_{EER} = 1.129$ ; and  $EER = 0.006, \lambda_{EER} = 0.729$ . As the frequency point where the RFF is significant is not regularly distributed, the extra FFT points obtained by higher point number may either pick up the significant RFF or just add more noise.

## V. CONCLUSION

In this work, we rigorously evaluate the influence of real-world constraints along every single step in the WPLI techniques, using a new theoretical model and in-lab experiments. The theoretical model provide the first systematical description on the whole WPLI procedure, which is applicable in most WPLI that based on digital wireless communications. The model is then implemented to comprehensively characterize various WPLI techniques that utilize the frequency domain RFF from the non-linear RF front-end, with different settings in transmitters, receivers, and wireless channels. From both theoretical deduction and experiment validation, we reveal

TABLE I  
GENERAL MATHEMATIC NOTATIONS.

Notations	Description
$x_m$	transmitted symbols
$T_{symbol}$	duration of each symbol
$\sigma_{TIE}^m$	time interval error (TIE)
$h_s(t, T_m)$	shaping filter
$b_{mod}(\cdot)$	function of modulation scheme
$T_g$	a generation period of DAC
$A$	amplitude coefficient of modulation
$u[n]$	baseband signal sequence
$u(t)$	time-continuous baseband signal
$y_u(t)$	output signal from DAC
$\Delta_n$	quantization noise
$[-U, U]$	input signal dynamic range
$\delta_\Delta$	maximum quantization error
$\Delta_{INL}$	integral nonlinearity
$z(t)$	complex passband signal
$\omega_c$	carrier angle frequency
$\zeta$	quadrature error
$w(t)$	output signal of the front-end amplifier
$h_{PA}(\cdot, \mathbf{a}_{tx})$	nonlinear function of power amplifier
$\mathbf{a}_{tx}$	complex complex power-series
$\otimes$	convolution computing
$h_{BP}(t)$	the bandpass filter function
$\hat{A}_{tx}(t)$	intensity of radiated EM waves by transmitter antenna
$\hat{\beta}_h, \hat{\beta}_v$	direction unit vectors in horizontal/vertical directions
$F_{tx}^h(\cdot), F_{tx}^v(\cdot)$	TX antenna projection functions
$\phi_{tx}^h, \phi_{tx}^v$	the polarization phases
$\hat{A}_{rx}(t)$	intensity of the EM waves at the RX antenna
$N_p$	number of paths
$h_i^h, h_i^v$	the path loss of the $i^{th}$ path
$\tau_i$	propagation delay of the $i^{th}$ path
$r(t)$	received passband signal
$F_{rx}^h(\cdot)^{-1}, F_{rx}^v(\cdot)^{-1}$	RX antenna functions
$\phi_{rx}^h, \phi_{rx}^v$	polarization phases of the RX antenna
$f(t)$	signal after RF front-end at the receiver
$x(t)$	received baseband signal
$h_{LP}(t)$	low pass filter
$A_p, A_s$	gains in the pass-band and stop-band
$x[n]$	digital signal sequences sampled by ADC
$\Delta_n$	random quantization noise of ADC
$T_s$	sampling period of ADC
$Feature(\cdot)$	feature extraction function
$\mathcal{H}_N$	hypothesis of signal is from the genuine user #N
$\lambda$	decision threshold
$N_{AWGN}$	channel background noise
$\alpha_{pl}$	large scale path loss
$\eta$	path loss exponent
$X_\sigma$	a normal random variable
$\alpha_{ch}$	small scale multipath fading
$I_0(\cdot)$	zeroth-order modified Bessel function of the first kind
$f_s$	the ADC sampling rate
$N_{FFT}$	number of FFT point number
$Q_u(\cdot)$	generalized Marcum Q-function
$\gamma$	SNR of difference vector over the Gaussian noise
$\mu$	time bandwidth product
${}_1F_1(\dots)$	the confluent hypergeometric function
$\Gamma(\cdot)$	the incomplete gamma function
$\kappa$	LDA dimension
$\mathbf{W}_{LDA}$	LDA feature training matrix

REFERENCES

- [1] B. Danev, D. Zanetti, and S. Capkun, "On physical-layer identification of wireless devices," *ACM Computing Surveys (CSUR)*, vol. 45, no. 1, p. 6, 2012.
- [2] Z. Li, W. Xu, R. Miller, and W. Trappe, "Securing wireless systems via lower layer enforcements," in *Proceedings of the 5th ACM workshop on Wireless security*. ACM, 2006, pp. 33–42.
- [3] R. Zhang, L. Song, Z. Han, B. Jiao, and M. Debbah, "Physical layer security for two way relay communications with friendly jammers," in *Global Telecommunications Conference (GLOBECOM 2010), 2010 IEEE*. IEEE, 2010, pp. 1–6.
- [4] J. Chen, R. Zhang, L. Song, Z. Han, and B. Jiao, "Joint relay and jammer selection for secure two-way relay networks," *Information Forensics and Security, IEEE Transactions on*, vol. 7, no. 1, pp. 310–320, 2012.
- [5] D. Zanetti, B. Danev et al., "Physical-layer identification of uhf rfid tags," in *Proceedings of the sixteenth annual international conference on Mobile computing and networking*. ACM, 2010, pp. 353–364.
- [6] S. Jana and S. K. Kaseria, "On fast and accurate detection of unauthorized wireless access points using clock skews," *Mobile Computing, IEEE Transactions on*, vol. 9, no. 3, pp. 449–462, 2010.
- [7] A. C. Polak, S. Dolatshahi, and D. L. Goeckel, "Identifying wireless users via transmitter imperfections," *Selected Areas in Communications, IEEE Journal on*, vol. 29, no. 7, pp. 1469–1479, 2011.
- [8] J. Toonstra and W. Kinsner, "A radio transmitter fingerprinting system odo-1," in *Electrical and Computer Engineering, 1996. Canadian Conference on*, vol. 1. IEEE, 1996, pp. 60–63.
- [9] —, "Transient analysis and genetic algorithms for classification," in *WESCANEX 95. Communications, Power, and Computing. Conference Proceedings., IEEE*, vol. 2. IEEE, 1995, pp. 432–437.
- [10] A. C. Polak and D. L. Goeckel, "Rf fingerprinting of users who actively mask their identities with artificial distortion," in *Signals, Systems and Computers (ASILOMAR), 2011 Conference Record of the Forty Fifth Asilomar Conference on*. IEEE, 2011, pp. 270–274.
- [11] M.-W. Liu and J. F. Doherty, "Specific emitter identification using nonlinear device estimation," in *Sarnoff Symposium, 2008 IEEE*. IEEE, 2008, pp. 1–5.
- [12] B. Danev, T. S. Heydt-Benjamin, and S. Capkun, "Physical-layer identification of rfid devices." in *Usenix Security Symposium*, 2009, pp. 199–214.
- [13] V. Brik, S. Banerjee, M. Gruteser, and S. Oh, "Wireless device identification with radiometric signatures," in *Proceedings of the 14th ACM international conference on Mobile computing and networking*. ACM, 2008, pp. 116–127.
- [14] L. Xiao, L. Greenstein, N. Mandayam, and W. Trappe, "Fingerprints in the ether: Using the physical layer for wireless authentication," in *Communications, 2007. ICC'07. IEEE International Conference on*. IEEE, 2007, pp. 4646–4651.
- [15] B. Danev and S. Capkun, "Transient-based identification of wireless sensor nodes," in *Proceedings of the 2009 International Conference on Information Processing in Sensor Networks*. IEEE Computer Society, 2009, pp. 25–36.
- [16] S. U. Rehman, K. Sowerby, and C. Coghill, "Rf fingerprint extraction from the energy envelope of an instantaneous transient signal," in *Communications Theory Workshop (AusCTW), 2012 Australian*. IEEE, 2012, pp. 90–95.
- [17] J. Hall, M. Barbeau, and E. Kranakis, "Enhancing intrusion detection in wireless networks using radio frequency fingerprinting." in *Communications, Internet, and Information Technology*, 2004, pp. 201–206.
- [18] W. C. Suski, M. A. Temple, M. J. Mendenhall, and R. F. Mills, "Using spectral fingerprints to improve wireless network security," in *Global Telecommunications Conference, 2008. IEEE GLOBECOM 2008. IEEE*. IEEE, 2008, pp. 1–5.
- [19] R. W. Klein, M. A. Temple, M. J. Mendenhall, and D. R. Reising, "Sensitivity analysis of burst detection and rf fingerprinting classification performance," in *Communications, 2009. ICC'09. IEEE International Conference on*. IEEE, 2009, pp. 1–5.
- [20] S. U. Rehman, K. Sowerby, C. Coghill, and W. Holmes, "The analysis of rf fingerprinting for low-end wireless receivers with application to ieee 802.11 a," in *Mobile and Wireless Networking (iCOST), 2012 International Conference on Selected Topics in*. IEEE, 2012, pp. 24–29.
- [21] M. Barbeau, J. Hall, and E. Kranakis, "Detection of rogue devices in bluetooth networks using radio frequency fingerprinting," in *Proceedings of the 3rd IASTED International Conference on Communications and Computer Networks, CCN*. Citeseer, 2006, pp. 4–6.

several key influence factors in real-world applications, including the constraints in wireless regulation, the origins of RFFs, the multipath fading channel and mobile users, and the sophistication of the receiver device. Our results show that existing WPLI techniques is less likely to achieve acceptable accuracy in real-world operation environments with off-the-shelf wireless devices, which motivate the discovery of new sources of more reliable and differentiable RFFs.

- [22] N. T. Nguyen, R. Zheng, and Z. Han, "On identifying primary user emulation attacks in cognitive radio systems using nonparametric bayesian classification," *Signal Processing, IEEE Transactions on*, vol. 60, no. 3, pp. 1432–1445, 2012.
- [23] M. D'Apuzzo, M. D'Arco, A. Liccardo, and M. Vadursi, "Modeling dac output waveforms," *Instrumentation and Measurement, IEEE Transactions on*, vol. 59, no. 11, pp. 2854–2862, 2010.
- [24] K. M. Gharaibeh, *Nonlinear distortion in wireless systems: modeling and simulation with Matlab*. John Wiley & Sons, 2011.
- [25] R. Y. Levine and T. S. Khuon, "Training-set-based performance measures for data-adaptive decisioning systems," in *San Diego'92*. International Society for Optics and Photonics, 1992, pp. 518–528.
- [26] A. C. Polak and D. L. Goeckel, "Identification of wireless devices of users who actively fake their rf fingerprints with artificial data distortion," *Wireless Communications, IEEE Transactions on*, vol. 14, no. 11, pp. 5889–5899, 2015.
- [27] K. G. Gard, L. E. Larson, and M. B. Steer, "The impact of rf front-end characteristics on the spectral regrowth of communications signals," *Microwave Theory and Techniques, IEEE Transactions on*, vol. 53, no. 6, pp. 2179–2186, 2005.
- [28] M. Datasheet, "Crossbow technology inc," *San Jose, California*, 2006.
- [29] M. Ettus, "Universal software radio peripheral (usrp)," *Ettus Research LLC* <http://www.ettus.com>, 2008.
- [30] M. K. Simon and M.-S. Alouini, *Digital communication over fading channels*. John Wiley & Sons, 2005, vol. 95.
- [31] I. F. Akyildiz and M. C. Vuran, *Wireless sensor networks*. John Wiley & Sons, 2010, vol. 4.
- [32] T. Lee and H. Ochiai, "Characterization of power spectral density for nonlinearly amplified ofdm signals based on cross-correlation coefficient," *EURASIP Journal on Wireless Communications and Networking*, vol. 2014, no. 1, pp. 1–15, 2014.
- [33] G. T. Zhou and J. S. Kenney, "Predicting spectral regrowth of nonlinear power amplifiers," *Communications, IEEE Transactions on*, vol. 50, no. 5, pp. 718–722, 2002.
- [34] A. S. Tehrani, H. Cao, A. Behravan, T. Eriksson, and C. Fager, "Successive cancellation of power amplifier distortion for multiuser detection," in *Vehicular Technology Conference Fall (VTC 2010-Fall), 2010 IEEE 72nd*. IEEE, 2010, pp. 1–5.
- [35] C.-L. Wang, T. I. Laakso, and J. E. Cousseau, "Receiver cancellation of nonlinear power amplifier distortion in sdma-ofdm systems," in *Acoustics, Speech and Signal Processing, 2006. ICASSP 2006 Proceedings. 2006 IEEE International Conference on*, vol. 4. IEEE, 2006, pp. IV–IV.
- [36] F. H. Gregorio, S. Werner, J. Cousseau, J. Figueroa, and R. Wichman, "Receiver-side nonlinearities mitigation using an extended iterative decision-based technique," *Signal Processing*, vol. 91, no. 8, pp. 2042–2056, 2011.
- [37] C. M. Bishop, *Pattern recognition and machine learning*. springer, 2006.
- [38] F. F. Digham, M.-S. Alouini, and M. K. Simon, "On the energy detection of unknown signals over fading channels," in *Communications, 2003. ICC'03. IEEE International Conference on*, vol. 5. IEEE, 2003, pp. 3575–3579.
- [39] T. Instruments, "Cc2420 datasheet," *Reference SWRS041B*, 2007.
- [40] K. B. Rasmussen and S. Capkun, "Implications of radio fingerprinting on the security of sensor networks," in *Security and Privacy in Communications Networks and the Workshops, 2007. SecureComm 2007. Third International Conference on*. IEEE, 2007, pp. 331–340.



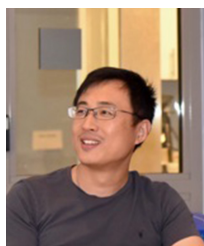
**Wenhao Wang** (S'16) received the B.S. degree in communication engineering from Southwest Jiaotong University (SWJTU), Chengdu, China, in 2011. He is currently pursuing the Ph.D degree with Prof. Bocheng Zhu at the School of Electronics Engineering and Computer Science, Peking University, Beijing, China. He is also a joint-training Ph.D. student with Prof. Zhi Sun at the Department of Electrical Engineering, State University of New York at Buffalo, Buffalo, NY, USA. Wenhao Wang was awarded the scholarship from China Scholarship

Council (CSC) for his study in USA in 2014. His research interests include wireless communication, physical-layer security, information-theoretic security, and radio frequency fingerprints.



**Zhi Sun** (M'11) received the B.S. degree in telecommunication engineering from Beijing University of Posts and Telecommunications (BUPT), Beijing, China, the M.S. degree in electronic engineering from Tsinghua University, Beijing, China, in 2004 and 2007, respectively, and the Ph.D. degree in electrical and computer engineering from Georgia Institute of Technology, Atlanta, GA, USA, in 2011. Currently, he is an Assistant Professor with the Department of Electrical Engineering, State University of New York at Buffalo, Buffalo, NY, USA. Prior

to that, he was a Postdoctoral Fellow with Georgia Institute of Technology, Atlanta, GA, USA. Prof. Sun was the recipient of the Best Paper Award in the 2010 IEEE Global Communications Conference (Globecom). He was also the recipient of the BWN Researcher of the Year Award at Georgia Institute of Technology in 2009, and the Outstanding Graduate Award at Tsinghua University in 2007. His research interests include wireless communication and networking in complex environments, metamaterial enhanced communication and security, physical-layer security, wireless intra-body networks, wireless underground networks, wireless underwater networks, and cyber physical systems.



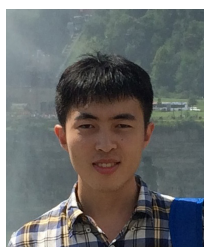
**Kui Ren** (M'07-SM'11-F'16) is a professor of Computer Science and Engineering and the director of UbiSeC Lab at State University of New York at Buffalo. He received his PhD degree from Worcester Polytechnic Institute. Kui's current research interest spans Cloud & Outsourcing Security, Wireless & Wearable Systems Security, and Mobile Sensing & Crowdsourcing. His research has been supported by NSF, DoE, AFRL, MSR, and Amazon. He was a recipient of SEAS Senior Researcher of the Year in 2015, Sigma Xi/IIT Research Excellence Award

in 2012, and NSF CAREER Award in 2011. Kui has published 150 peer-review journal and conference papers and received several Best Paper Awards including IEEE ICNP 2011. He currently serves as an associate editor for IEEE Transactions on Dependable and Secure Computing, IEEE Transactions on Mobile Computing, IEEE Wireless Communications, IEEE Internet of Things Journal, and IEEE Transactions on Smart Grid. Kui is a Fellow of IEEE, a Distinguished Lecturer of IEEE, a member of ACM, and a past board member of Internet Privacy Task Force, State of Illinois.



**Bocheng Zhu** received the Ph.D. degree in electromagnetic field and microwave technology from Beijing Institute of Technology, Beijing, China, in 1996. Currently, he is a professor at the School of Electronics Engineering and Computer Science, Peking University, Beijing, China. Prof. Zhu is a senior member in Chinese Institute of Electronics. He is also a senior reviewer of the National High Technology Research and Development Program (863 program) and the National Science and Technology Major Project of China. His research

interests include wireless communication, satellite navigation and microwave technology.



**Sixu Piao** received the B.S. degree in Computer Science and Engineering from the University of Science and Technology of China (USTC), Hefei, China, in 2014. He is currently pursuing the Ph.D degree with Prof. Kui Ren in the Department of Computer Science and Engineering, University at Buffalo, Buffalo, NY, USA. His research interests include security and privacy in mobile sensing, physical layer authentication and optimized sensing & mapping with UAV.